ANOMALOUS TRANSPORT BY KELVIN-HELMHOLTZ INSTABILITIES

Akira Miura

Geophysics Research Laboratory, University of Tokyo
Bunkyo-ku, Tokyo, 113, Japan

ABSTRACT

Simulation of magnetohydrodynamic Kelvin-Helmholtz instabilities has been performed for parallel ($B_0 \parallel V_0$) and transverse ($B_0 \perp V_0$) configurations, modeling high latitude (or downstream flanks) and dayside low latitude magnetospheric boundaries. In the parallel configuration, a super-Alfvénic and trans-sonic shear flow develops into small eddies, which strongly compresses, twists, and hence amplifies the magnetic field by the dynamo action with an amplification factor $M_A/2$. In the nonlinear stage, however large the initial Alfvén mach number M_A may be, the magnetic field amplified and twisted by the hydromagnetic flow vortices reacts back upon the flow evolution, and the flow vortices cascade into smaller structures. In the transverse configuration the instability leads to the formation of a fast shock discontinuity from an initially sub-fast shear flow. Anomalous tangential stress by the instability in the transverse configuration reaches 1% of the magnetosheath momentum flux, but for the parallel configuration, the anomalous transport is 2-3 times larger than the anomalous transport in the transverse configuration. The anomalous transport for both configurations satisfies the requirement of the viscous-like interaciton at the mangetospheric boundary.

1. INTRODUCTION

The Kelvin-Helmholtz (K-H) instability is important in understanding a variety of space and astrophysical phenomena involving sheared plasma flow. Of particular interest in the space plasma is the consequence of the Kelvin-Helmholtz instability in the hydromagnetic interaction between solar wind and magnetosphere at the magnetosphere boundary (Figure 1): It has long been suggested that at the magnetospheric boundary the Kelvin-Helmholtz instability is excited by velocity shears and leads to a "viscous-like" interaciton

(Axford and Hines, 1961) at the boundary, i.e., the net transport of solar wind momentum and energy into the magnetosphre, in order to drive the large-scale plasma convection inside the magnetosphere. Most of theoretical attempts in the past on the Kelvin-Helmholtz instability have been directed to the linear analysis and have been successful in showing that the magnetospheric boundary is linearly unstable for the Kelvin-Helmholtz instability; however, there has been no self-consistent nonlinear treatment of the instability, which could answer what nonlinear state is realized and how much momentum and energy is tranfered by the instability into the magnetosphere, a question being particularly of interest in understanding energetics of the solar wind-magnetosphere interaction.
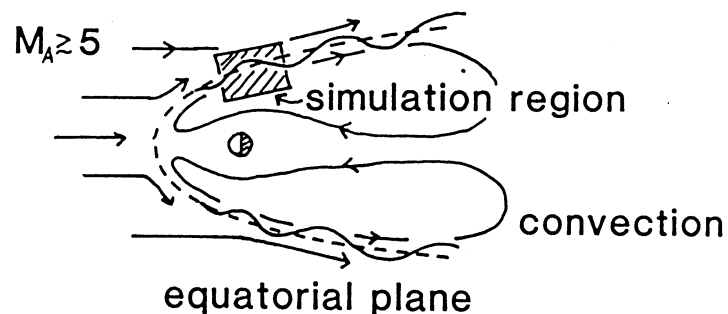

Figure 1.   Solar wind-magnetosphere interaction in the equatorial plane.

In this paper we study by means of magnetohydrodynamic (MHD) simulation the MHD Kelvin-Helmholtz instability in a compressible plasma as an initial value problem. By such a self-consistent nonlinear treatment, we will be able to elucidate the basic nonliear dynamics of the instabilities (Miura, 1982) in the basic configurations of sheared plasma flow and magnetic field and answer how much momentum and enrgy of the solar wind is transfered into the magnetosphere by the Kelvin-Helmholtz instabilities at the magnetospheric boundaries.

2.   BASIC EQUATIONS AND MODELS

The conservative form of the ideal MHD equations, which describe the hydromagnetic Kelvin-Helmholtz instability are:

$$\frac{\partial \rho}{\partial t} = - \underset{\sim}{\nabla} \cdot (\rho \underset{\sim}{v}) \tag{1}$$

$$\frac{\partial}{\partial t} (\rho \underset{\sim}{v}) = - \underset{\sim}{\nabla} \cdot (\rho \underset{\sim\sim}{vv} - \frac{1}{\mu_0} \underset{\sim\sim}{BB}) - \underset{\sim}{\nabla} (p + \frac{B^2}{2\mu_0}) \tag{2}$$

$$\frac{\partial \underset{\sim}{B}}{\partial t} = \underset{\sim}{\nabla} \times (\underset{\sim}{v} \times \underset{\sim}{B}) \tag{3}$$

$$\frac{\partial \varepsilon}{\partial t} = - \underset{\sim}{\nabla} \cdot [(\varepsilon + p + \frac{B^2}{2\mu_0}) \underset{\sim}{v} - \frac{1}{\mu_0} (\underset{\sim}{B} \cdot \underset{\sim}{v}) \underset{\sim}{B}] \tag{4}$$

here, ρ, $\underset{\sim}{v}$, $\underset{\sim}{B}$, and p are the plasma mass density, bulk velocity of the plasma, magnetic field and plasma pressure, and ε is the energy density defined by

$$\varepsilon = \frac{1}{2} \rho v^2 + \frac{1}{2\mu_0} B^2 + \frac{P}{\gamma - 1} \tag{5}$$

We show in Figure 2 the two basic configurations of the instability in a uniform magnetic field B_0 investigated in the present simulation. The parallel configuration models the magnetospheric boundary at high latitudes in the noon-midnight meridian plane or the downstream flanks, where the magnetic field has a large component parallel to the sheared plasma flow. The transverse configuration models the magnetospheric boundary at the dayside low latitude near the equatorial plane, where the magnetic field is almost transverse to the sheared plasma flow. The parameters which appear in the following simulation are the sound mach number $M_S = V_0/c_S$ and the Alfvén mach number $M_A = V_0/v_A$, where V_0 is the total jump of the velocity across the shear layer, c_S and v_A being the sound speed and Alfvén speed, respectively. Regarding stability of the velocity shear layer in the parallel configuration we should notice that the tension of the magnetic field lines sets the following instability condition for K-H instability

$$M_A > 2 \tag{6}$$

By using these simple configurations and parameters, we will be able to elucidate the basic nonlinear dynamics of the instability involved in the above two basic configurations and their parametric dependence, which are applicable not only to magnetospheric boundary but also to wide regions of space and astrophysical problems. For the velocity profile we assume a hyperbolic tangent form,

$$v_{oy}(x) = - (V_0/2) \tanh(x/a) \tag{7}$$

characterized by a total velocity jump V_0 and velocity shear scale length a.

Parallel Configuration

(a)

$V_0(x)$

B_0

Transverse Configuration

(b)

B_0

V_0

$\Delta = 2a$

$V_0(x)$

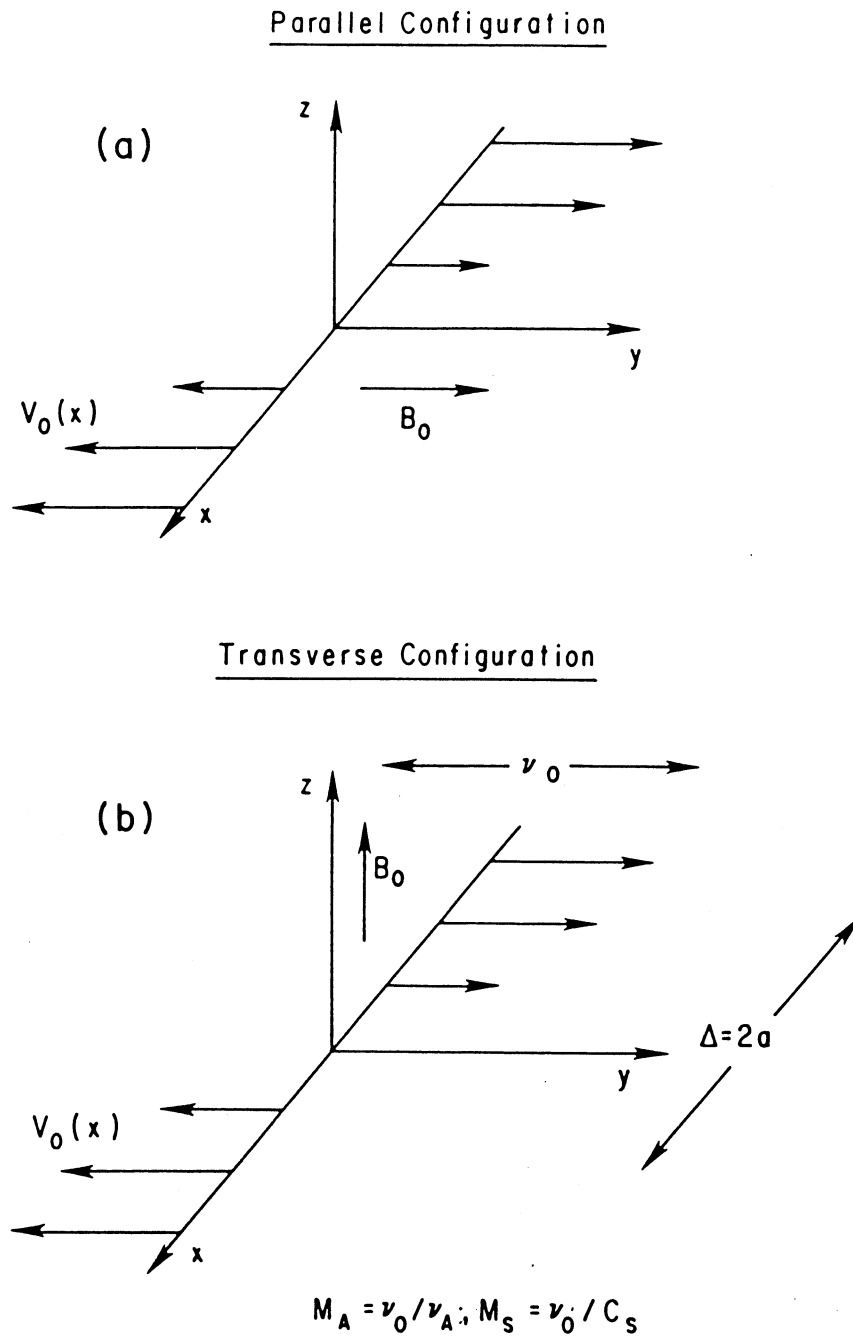$M_A = V_0 / V_A$; $M_S = V_0 / C_S$

Figure 2. Two basic configurations of the MHD Kelvin-Helmholtz
instability. The magnetic field is either parallel to the
flow (parallel con-figuration) or perpendicular to the flow
(transverse configuration). The velocity profile is
characterized by a total velocity jump V_0 and a scale
length 2a.

3. NUMERICS

Simulations are performed in the x-y plane where the initial flow velocity v_y has a shear profile in the x direction. We impose a boundary condition such that there is no mass flow ($v_x=0$) across boundaries at $x=\pm x_b$ and all quantities are periodic in the y direction. It then follows from (1)-(4) that B_x and derivatives with respect to x of the remaining quantities ($\rho, v_y, v_z, B_y, B_z, p$) must vanish at the boundaries ($x=\pm x_b$). This boundary condition means that the flow kinetic energy flux and the poynting flux across the boundaries vanish. Therefore, there is no inflow and outflow of energy across the boundaries. For the present simulation we have placed the boundaries at $x=\pm 10a$, which is far enough from the shear region to make boundary effects negligible. In the following time is normalized by $\tau=2a/V_0$, and we use a mesh system with a (100,100) mesh.

In the present simulation we have given a linearly unstable perturbation at the initial stage (t=0) as an initial seed of the growing perturbation. Such a linearly unstable perturbation was obtained by linear eigenmode analysis by the initial value code (Miura and Pritchett, 1982), which follows the linearized MHD equation numerically to produce the linear eigenmode. We have used the two-step Lax-Wendroff scheme (Richtmyer and Morton, 1967) to solve equations (1)-(4) and a mesh system with a (100,100) mesh. Although the Lax-Wendroff scheme includeds an artificial viscosity term implicitly, it turned out during the computation that the artificial viscosity only by the Lax-Wendroff scheme was not enough to smooth the final MHD solution and a large mesh oscillation was actually observed. Therefore, we have added additional artifical viscosity term following Lapidus (1967) in order to smooth the solution and provide a dissipation mechanism, which is necessary to resolve a fast shock discontinuity generated by the K-H instability. Namely, following Lapidus (1967), we have added artificial viscosity term to the MHD variables first by smoothing those variables in x direction and then smoothing them in y direction as follows:

$$\underset{\sim}{V}^1 = \frac{\Delta t}{\Delta x} \frac{\kappa}{4} [\ |u^1_{x+2\Delta x,y} - u^1_{x,y}|\ (\ \underset{\sim}{U}^1_{x+2\Delta x,y} - \underset{\sim}{U}^1_{x,y}\ )$$
$$- |u^1_{x-2\Delta x,y} - u^1_{x,y}|\ (\ \underset{\sim}{U}^1_{x,y} - \underset{\sim}{U}^1_{x-2\Delta x,y}\ )\ ] \tag{8}$$

$$\underset{\sim}{U}^2 = \underset{\sim}{U}^1 + \underset{\sim}{V}^1 \tag{9}$$

$$\underset{\sim}{V}^2 = \frac{\Delta t}{\Delta y} \frac{\kappa}{4} [\ |v^2_{x,y+2\Delta y} - v^2_{x,y}|\ (\ \underset{\sim}{U}^2_{x,y+2\Delta y} - \underset{\sim}{U}^2_{x,y}\ )$$
$$- |v^2_{x,y-2\Delta y} - v^2_{x,y}|\ (\ \underset{\sim}{U}^2_{x,y} - \underset{\sim}{U}^2_{x,y-2\Delta y}\ )\ ] \tag{10}$$

$$\underset{\sim}{U}^3 = \underset{\sim}{U}^2 + \underset{\sim}{V}^2 \tag{11}$$

where $u=v_x$, $v=v_y$, $\underset{\sim}{U}=(\rho,v_x,v_y,v_z,B_x,B_y,B_z,p)$, $\underset{\sim}{V^1}$ and $\underset{\sim}{V^2}$ are added artificial viscosity terms, suffixes 1-3 represent one cycle of each time step, and κ is a constant of order of unity. We have to be specially careful in such a smoothing process, however, since we try to elucidate the anomalous momentum transport or the anomalous viscosity induced by the Kelvin-Helmholtz instabilities, which is due to the finite large amplitude K-H mode. Therefore, by trial and errors, we have made those artificial viscosity terms as small as possible.

4. NUMERICAL RESULTS

4.1 Parallel configuration

First, we show results of a simulaiton run performd for the parallel configuration. Solid and dashed curves in Figure 3 marked by the symbol ‖ show the time evolution of normalized peak amplitudes
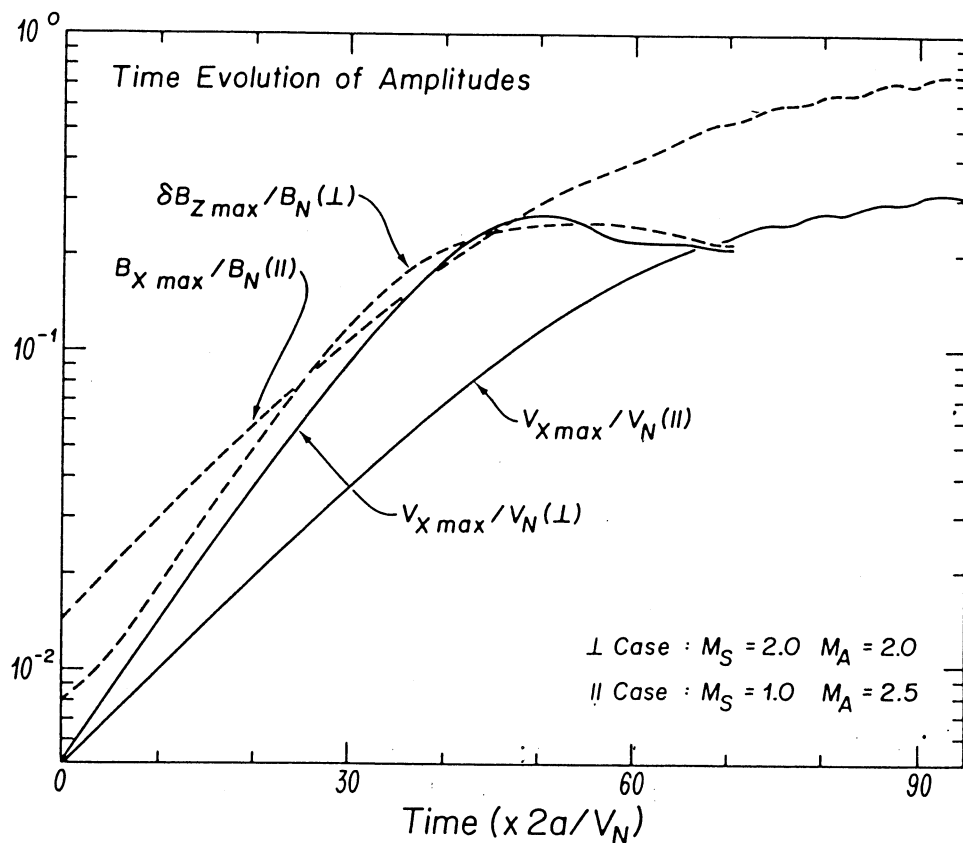

Figure 3. Time evolution of maximum normalized transverse velocity (solid curves) and maximum normalized compressional component of the magnetic field (dashed curves) for the parallel configuration with $M_S=1.0$, $M_A=2.5$ and the transverse configuration with $M_A=M_S=2.0$. Time is normalized by $2a/V_0$.

$V_{x\ max}/V_N$ and $B_{x\ max}/B_N$, where $B_N=B_0$ and $V_N=V_0$, for the parallel configuration with $M_S=1.0$, $M_A=2.5$. In the early stage, the amplitude grow linearly with the predicted linear growth rate. At $t/\tau=90$ the instability saturates, $V_{x\ max}/V_N$ reaches 30 %, and the magnetic field perturbation (transverse component) becomes comparable to the initial beckground magnetic field intensity.
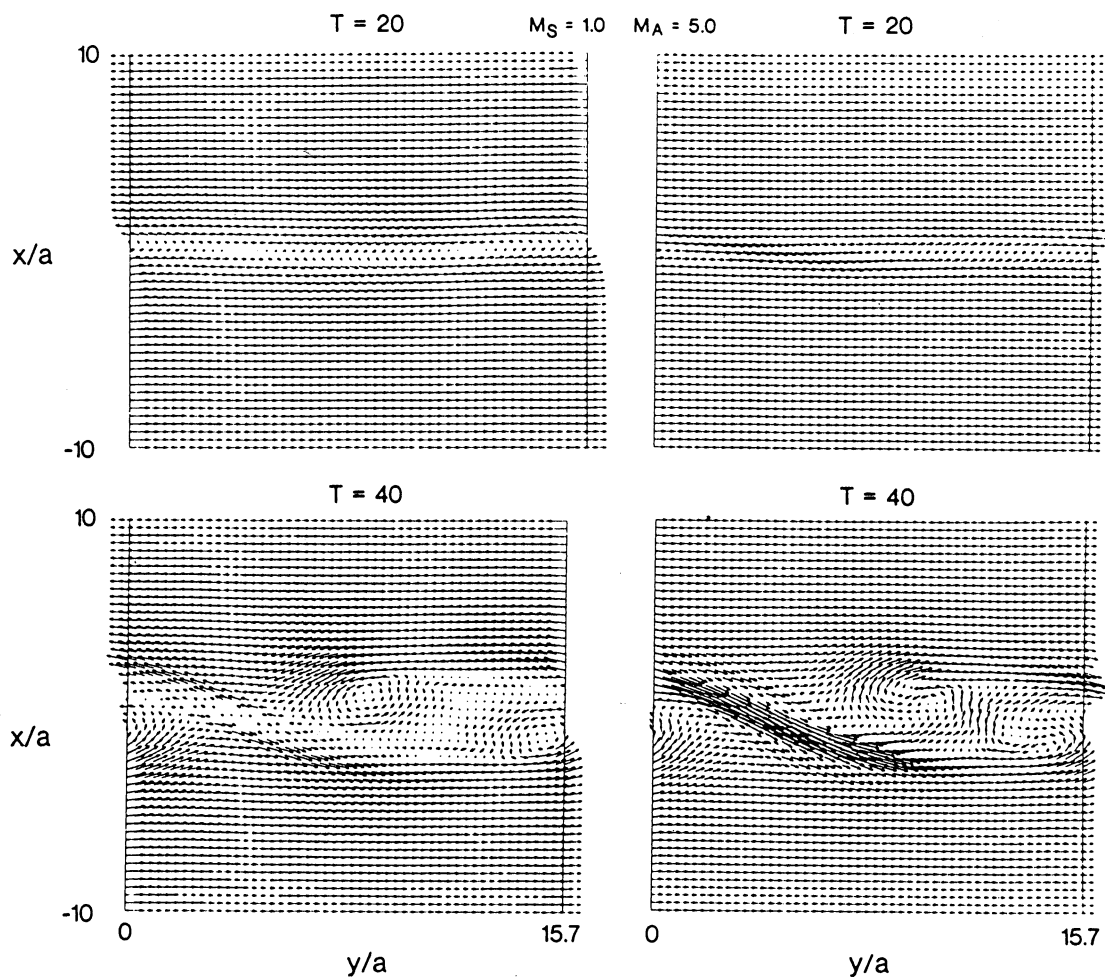

Figure 4.   Flow velocity (left) and magnetic field (right) at $t/\bar{\tau}=20$ and 40 for the parallel configuration ($M_S=1.0$, $M_A=5.0$).

Figure 4 shows flow vectors (left panels) and magnetic field vectors (right panels) at $t/\tau=20$ and 40 for a simulaiton run with $M_S=1.0$ and $M_A=5.0$. System length in the y direction L_y in this case is equal to $L_y=15.7a$, which corresponds to the wavelength of the fastest growing mode. In the early state ($t/\tau=20$), the sheared plasma

flow undulates slightly with the development of the instability (top left panel). Since the magnetic field is frozen into the plasma, the above undulaiton of the plasma flow leads to a slight bending of the magnetic field lines as seen in the top right panel. The shear flow is extremely disturbed, however, by the saturation stage $t/\tau=40$, and a pair of eddies is formed inside a large vortex at $7a<y<15.7a$. In the center of the large vortex, the flow is almost stagnant. A stagnation region also appears in between the large vortices, and the plasma flow toward this stagnation region induced by vortices is forced to diverge along a layer formed tangent to the vortices. The initially uniform magnetic field is slightly sheared and compressed inside the velocity shear layer at $t/\tau=20$ and eventually at $t/\tau=40$, a strong compression of the magnetic field occurs at $0<y<7a$ along the layer formed tangent to vortices. On the other hand at $7a<y<15a$ the magnetic field line is stretched and twisted strongly as a consequence of the wrapping-up of the field lines by the differential rotation associated with each of the twin vortices. In this case, the total magnetic energy in the whole calculation domain increased by 26 % of the initial total magnetic energy at the expense of the initial flow kinetic energy.

Shown in the upper panels of Figure 5 are 3-D views of the pressure distributions for this case. Initially the pressure was uniform, but with time, the pressure decreases along the region where the mangnetic flux tube is compressed on both sides. A substantial depletion of the plasma pressure is seen for later stage along the compressed flux tube formed tangent to vortices. This is because the flux tube is compressed on both sides by the incoming plasma flow induced by the vortex motion causing the plasma inside to be squeezed out of the flux tube.

In the bottom panel of Figure 5, we summarize plasma dynamics involved in the parallel configuration for the present case of $M_A=5.0$, which has led to a strong compression and twisting of magnetic field lines and the formation of a slow rarefaction layer. Illustrated also in this figure is an amplification of the magnetic field at the site of small eddies by the dynamo action, $E \cdot J = v \cdot (J \times B) < 0$, where E and J are the electric field and current induced by eddy motion and field line twisting. At the site of the slow rarefaction layer, the magnetic field is also amplified by slow magnetosonic rarefaction due to accumulation of magnetic field lines by flux transfer associated with frozen-in vortex motion. Both of these processes, i.e., twisting and compression of magnetic field lines, contribute to a dynamo mechanism, whereby the flow kinetic energy is converted into magnetic energy by a deceleration of the flow by the $J \times B$ magnetic force.

In order to see the dependence of the instability consequences on the Alfvén mach number M_A, we have performed simulation runs for $M_A=2.5$ and 10.0 and for a fixed sound mach number $M_S=1.0$. We show in Figure 6, flow velocity vectors at the saturation stage of the instability for $M_A=2.5,5.0,10.0$ from the top. For $M_A=2.5$, the tension of the magnetic field line is large in comparison with the inertial term and therefore the flow is only slightly undulated with twin eddy-

like circulations developed in a large vortex. With the increase of the mach number M_A, the flow is disturbed more and more and for $M_A=10.0$, a large vortex initially formed cascade into smaller eddies and the flow is more "turbulent" in the sense that the flow perturbation is now of much smaller scale size. The three panels in Figure 7 show magnetic field vectors corresponding to those flow vectors in Figure 6. For $M_A=2.5$, the magnetic field lines oscillate
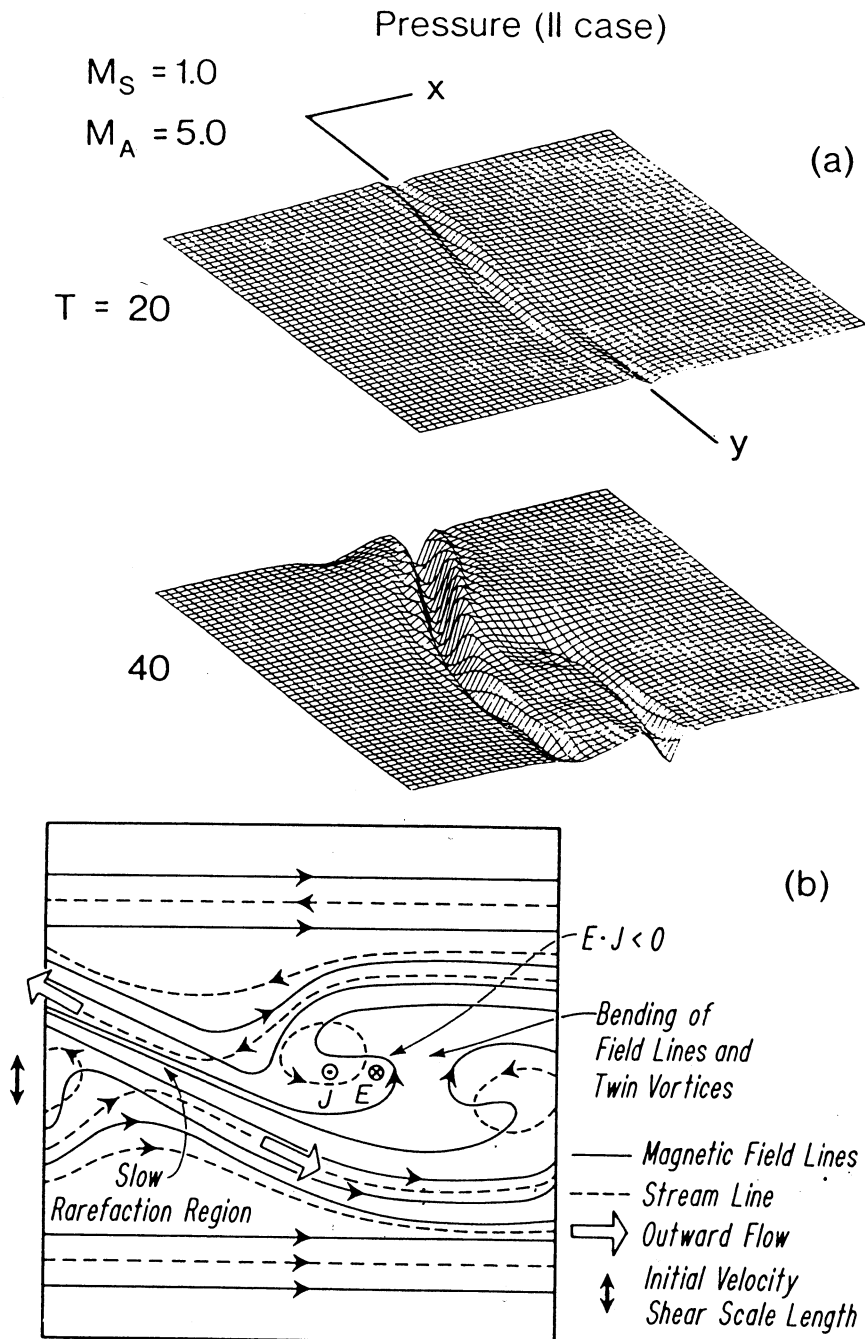

Figure 5.   Upper panels; three-dimensional plots of the pressure (top surface) at $t/\tau=20$ and 40 for the parallel configuration. Lower panel; plasma dynamics in the parallel configuration.
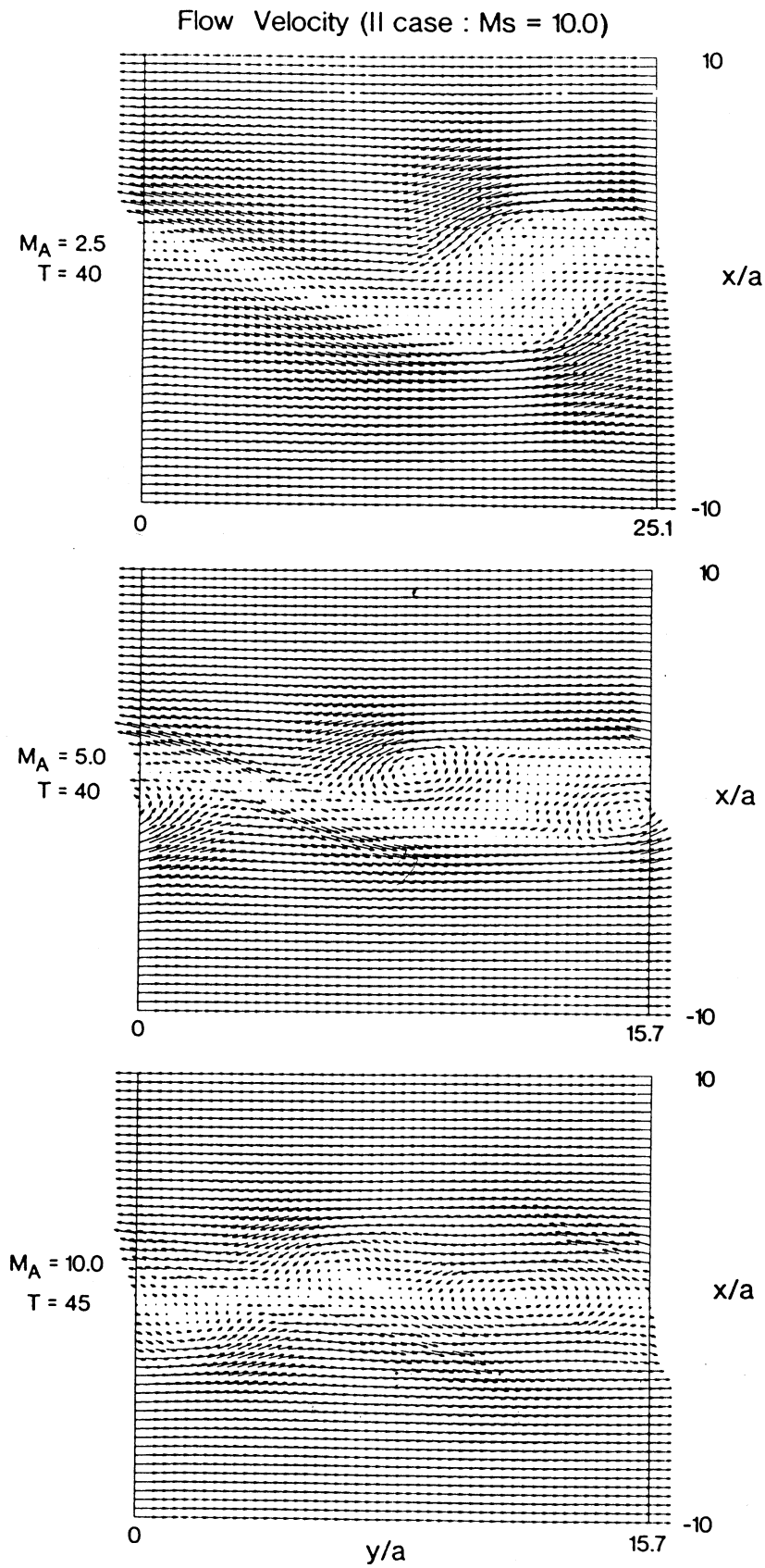
A. Miura

Flow Velocity (II case : Ms = 10.0)

Figure 6. Flow velocities . for three different Alfvén mach numbers
            $(M_A=2.5,5.0,10.0,$ and $M_S=1.0)$ in   the   parallel
            configuration.

Magnetic Field (II case : Ms = 1.0)
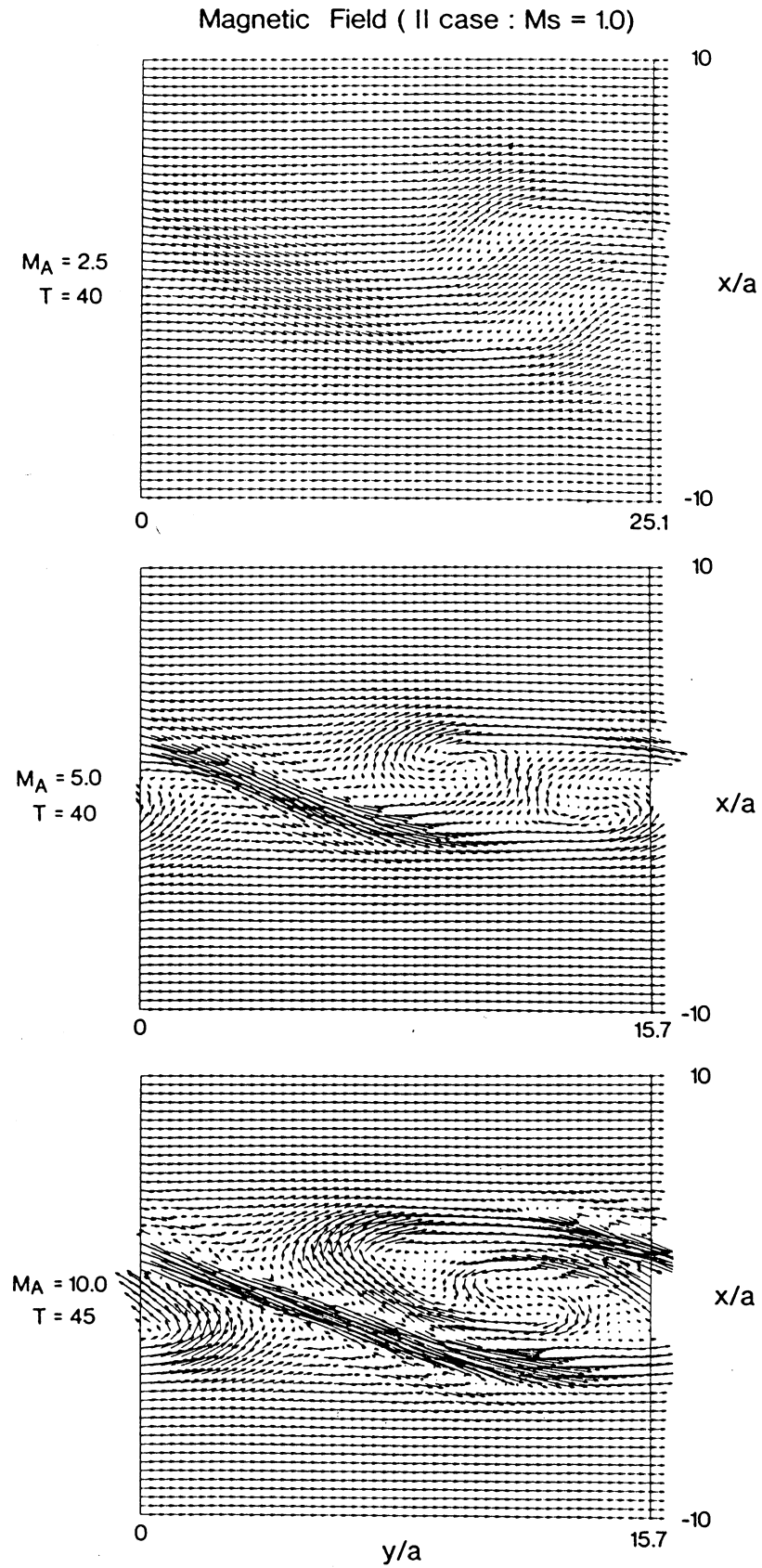

Figure 7.   Magnetic fields for three different Alfvén mach numbers (M_A= 2.5,5.0,10.0, and M_S=1.0) in the parallel configuration.

back and forth slightly owing to the frozen-in vortex motion inducedby
the instability. However, with the increase of M_A, the magnetic field
line is more strongly compressed and twisted by the flow vortices and
for $M_A=10.0$, the magnetic field is amplified six times of the initial
magnetic field in the slow rarefaction layer, and twisted several
times. Notice regarding the present numerical scheme that in the
middle and bottom panels, regions of magnetic field reversal are
formed, but they are not subject to reconnection by the numerical
resistivity. This fact provides us with a proof of the soundness of
the present numerical scheme for the ideal MHD plasma.

By a compression and twisting of the magnetic field line, the
magnetic energy in the whole calculation domain has increased (dynamo
action). In order to see this increase of the magnetic energy, we have
plotted in Figure 8 the time evolution of the relative magnetic energy
increase $[W_B-W_B (t=0)]/W_B (t=0)$ and the relative decrease of the flow
kinetic energy $[W_k-W_k (t=0)]/W_k (t=0)$. It is obviously seen in these
plots that the total magnetic energy in the whole calculation domain
increases exponentially with time at the expense of the flow kinetic
energy. This provides a solid evidence of the dynamo action by the K-
H instability in the parallel configuration. Both compression and
twisting of magnetic field lines contribute to a dynamo mechanism,
whereby the flow kinetic energy is converted into magnetic energy.
This dynamo process is caused by a deceleration of the flow by the JxB
magnetic force; that is, the magnetic field gains its energy from the
vortex flow by $\underset{\sim}{v}\cdot(\underset{\sim}{J}\times\underset{\sim}{B})<0$. For the present parameter ($M_S=1.0$), it is
obvious from Figure 7 that the magnetic field amplification by slow
rarefaction process contributes most to the increase in the magnetic
field. The efficiency of the magnetic field amplification using this
process depends on the Alfvén mach number M_A or the plasma
$\beta (\beta\simeq M_A^2/M_S^2)$. If we assume a quasi stationaly state, the amplification
factor of the magnetic field, i.e., B_f/B_i, where B_i is the initial
uniform magnetic field ($=B_0$) and B_f is the final magnetic field
strength inside the slow rarefaction layer, may be calculated as
follows: The lower panel in Figure 5 shows that the slow rarefaction
layer is formed as a consequence of the compression of the magnetic
flux tube by the incoming plasma flow induced by vortices. The
pressure balance between the inside and outside of the slow
rarefaction layer becomes

$$P_{out} + \rho_{out} v_{out}^2 + \frac{B_{out}^2}{2\mu_0} \sim P_{in} + \frac{B_{in}^2}{2\mu_0} \qquad (12)$$

where v_{out} is the velocity of the incoming plamsa flow, which is
almost normal to the slow rarefaction layer. From simulation results,
we found that $P_{out}-P_{in}<<\rho_{out}v_{out}^2$. Therefore, the above pressure
balance condition gives simply

$$\rho_{out} v_{out}^2 \sim \frac{B_{in}^2}{2\mu_0} \qquad (13)$$

This relation means that the dynamic pressure by the incoming plasma
flow is nearly balanced by the magnetic pressure inside the

rarefaction layer.   If we use the empirical fact obtained from simulation results

$$v_{out} \sim v_{x\ max} \sim \frac{V_O}{3} \qquad (14)$$

(13) can be rewritten as

$$\rho_{out}\ (\frac{V_O}{3})^2 \sim \frac{B_{in}^2}{2\mu_O} \qquad (15)$$

Thus, we can conclude that the amplification factor of the magnetic field is

$$\frac{B_f}{B_i} = (\ \frac{B_f^2/2\mu_O}{B_i^2/2\mu_O}\ )^{1/2} \sim (\ \frac{\rho_O(V_O/3)^2}{B_i^2/2\mu_O}\ )^{1/2} \sim \frac{1}{2}\ M_A \qquad (16)$$

We show in Table 1 the amplification factors,   obtained   from simulations and calculated from (16), of the magnetic field for three
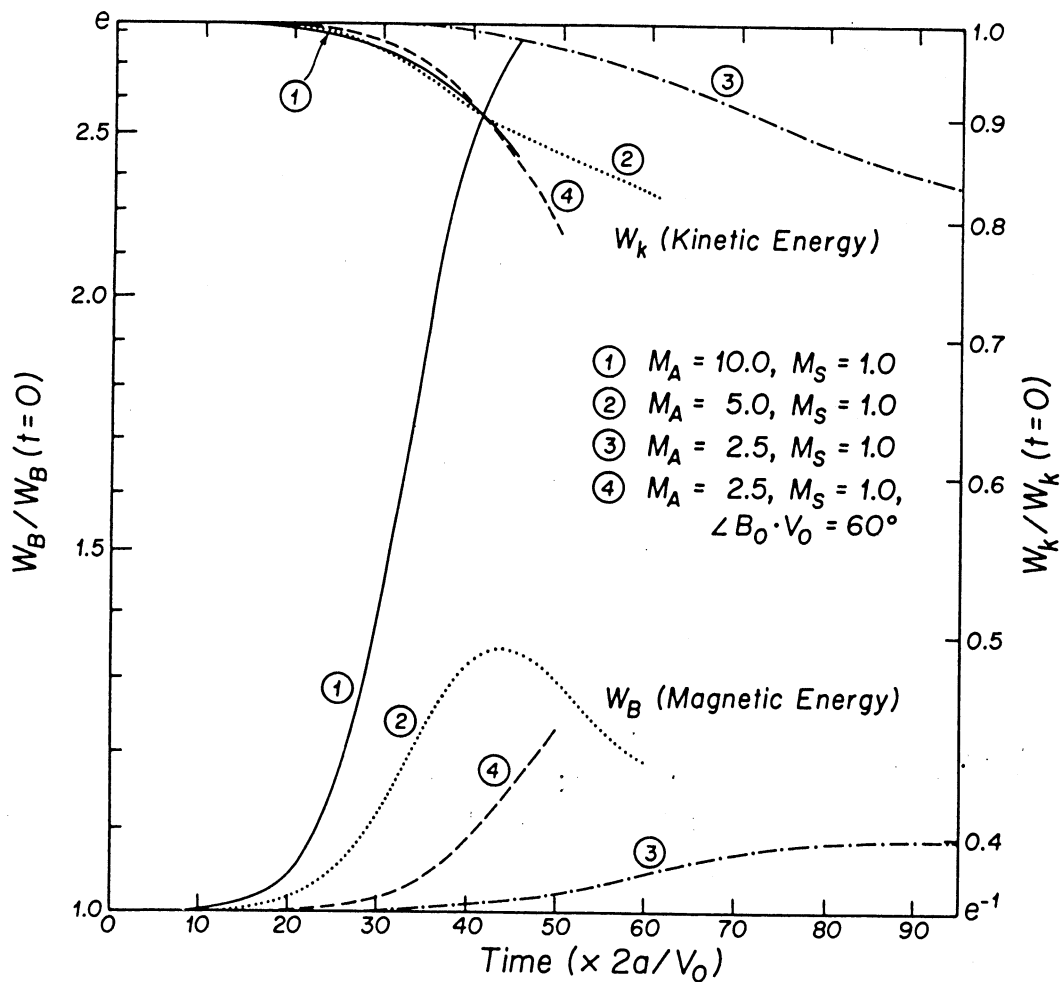

Figure 8. Time evolutions of total magnetic and kinetic energies in the whole calculation domain.

different values of M_A in the saturation stage. Although the above
calculations are based on a crude argument, the calculated
amplification factor has agreed very well with the simulation results,
suggesting that a simple dynamo relation (13) by slow magnetosonic
rerefaction is well satisfied in the actual simulation results.
Summarized also in Table 1 are the value of the initial plasma β and
that of the plasma β within the slow rarefaction layer at the
saturation stage for three different values of M_A. Although the
initial plasma β is much larger than unity for all cases, the plasma β
at its saturation stages becomes 1-2 for all cases, owing to the
squeezing process. Because of this large decrease of the plasma β
within the rarefaction layer, ∇p and $J \times B$ forces become almost
comparable, and hence the flow is strongly affected by the magnetic
field, even though the initial (seed) magnetic field satisfying $\beta \gg 1$
is too weak to affect the plasma motion.

4.2 Transverse configuration

Solid and dashed curves in Figure 8 marked by the sign⊥ show the
time evolution of normalized peak amplitudes $v_{x\ max}/V_N$, $B_{z\ max}/B_N$ for
the transverse configuration with $M_S=M_A=2.0$ ($M_f=1.44$), where M_f is the
fast magnetosonic mach number defined by $M_f=V_0/(c_S^2+v_A^2)^{1/2}$. Both
amplitudes grow linearly with the predicted linear growth rate $\tau=$
$0.09 \cdot 2a/V_0$. In the saturation stage, both normalized amplitudes reach
25%. In this case, the total magnetic field energy increased only
slightly, by 1.6 % of the initial total magnetic field energy by the
fast compression.

We show in Figure 9 simulation results of the transverse
configuration with its time evolution shown in Figure 3. The system
length L_y in this case is equal to 17.9a, which is equal to the
wavelength of the fastest growing mode λ. Left panels show flow
pattern at $t/\tau=25,55$. The initially laminar sheared plasma flow is
disturbed slightly at $t/\tau=25$, and it develops into a flat vortex cell
at $t/\tau=55$. This time evolution may be regarded in the magnetospheric
inertial frame as a spatial evolution along the magnetospheric
boundary from upstream to downstream over a distance of $55\tau \times 1/2V_0 \sim 3\lambda$
where λ is the wavelength of the fastest growing mode. The transverse
vortex size at $t/\tau=55$ becomes much larger than the initial thickness
of the velocity shear layer (2a), and therefore a large scale mixing
of plasma is accomplished by a vortex motion. It is seen that the
initial laminar shear flow is accelerated and decelerated periodically
in the y-direction, since the perturbed vortex motion periodically
changes the direction of rotation. Notice that the ultimate energy
for this acceleration is provided by the inertial force $\rho_0(\partial v_y/\partial x)v_x$
due to the velocity shear. An interesting consequence of the
instability found for this case is the formation of a pair of fast
shock structures aligned side by side across the velocity shear layer,
even though the initial maximum flow speed was less than the
magnetosonic speed ($v_{y\ max}=V_0/2=0.71\ V_f$). The right panels in Figure
9 show a 3-D view of the pressure distribution. It is seen that at
$t/\tau=55$, the pressure gradient presents a clear-cut discontinuity,

which appears at the strongly accelerated flow region in the bottom left panel. The physical picture leading to this fast shock formation is as follows: Initially, the plasma was uniform and the maximum flow
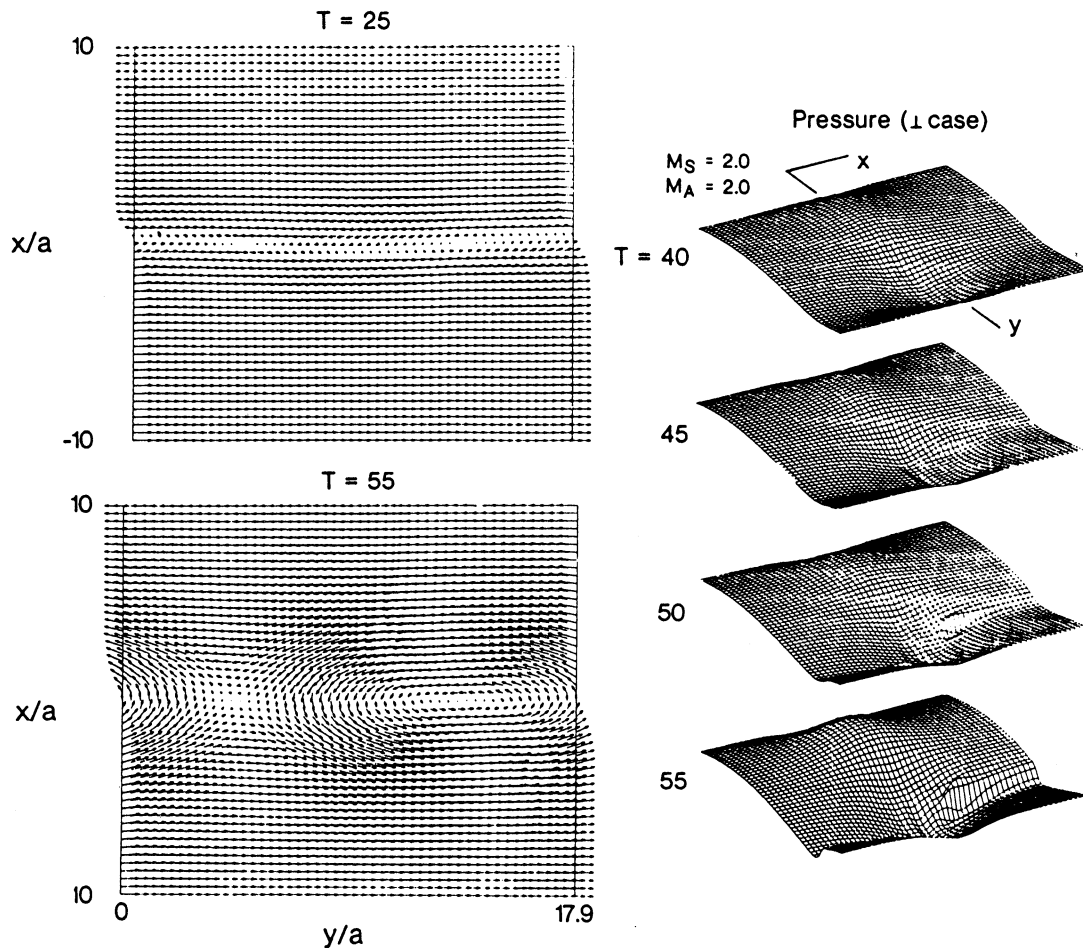

Figure 9. Flow velocity at $t/\tau=25$ and 55 (left panels) and three-dimensional plots of the pressure distribution (right panels) at $t/\tau=40,45,50,55$ for the transverse configuration $(M_S=M_A=2.0)$.

speed was below the magnetosonic speed. As the instability grows, however, the vortices are excited and the flow is accelerated and decelerated periodically in the y direction by the perturbed vortex motion. Therefore, the decelerated flow is overtaken by the accelerated flow causing the pressure gradient to steepen more and more with time. Eventually, the accelerated flow speed exceeds the local magnetosonic speed, and a fast shock discontinuity is formed.

In order to resolve the fast shock structure, we show in Figure 10 profiles in the y direction of pressure (p), density (ρ), and temperature (T) normalized by their initial values $p_N = p_0$, $\rho_N = \rho_0$, $T_N = T_0$, and profiles of V_y and the magnetosonic speed $(c_S^2 + v_A^2)^{1/2}$ normalized by V_0 at x=3.0a in the saturation stage (t/τ=55). At y=10a, those quantities present clear-cut discontinuities, across which the flow speed changes from super-fast (M_f=1.09) in the upstream side to sub-fast (M_f=0.7) in the downstream side, consistent with the shock condition (Landau and Lifshitz, 1959). Notice that in the present MHD scheme the dissipation mechanism necessary for the formation of the fast shock discontinuity is provided by the artificial viscosity implicitly included in the Lax-Wendroff scheme and that introduced following Lapidus (1967).
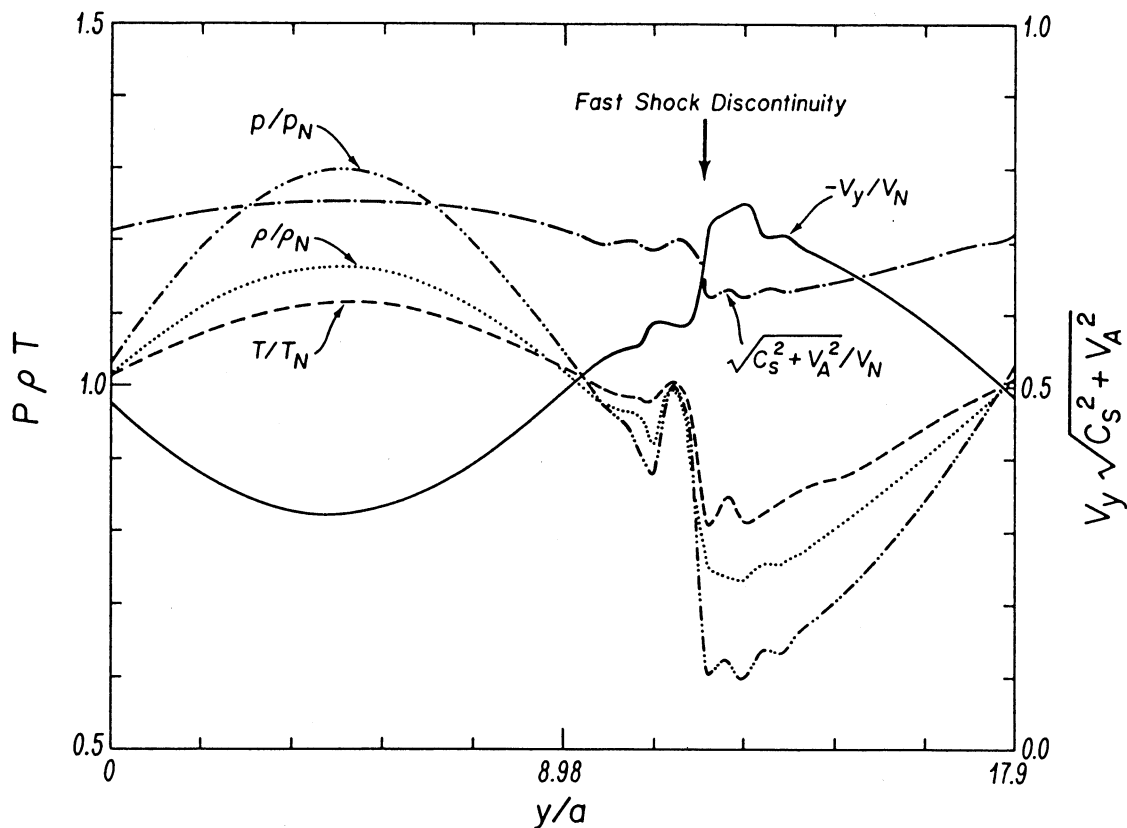

Figure 10. Profiles in the y-direction of pressure (p), density (ρ), temperature (T) normalized by their initial values p_N, ρ_N, T_N, and profiles of v_y and the magnetosonic speed normalized by V_0 for the transverse configuration ($M_S = M_A = 2.0$) at x=30a and T/τ=55.

It is obvious in Figure 10 that the initial uniform flow velocity (v_y) is perturbed and steepened to form a fast shock discontinuity where this velocity exceeds the local magnetosonic speed. The maximum perturbation of v_y becomes about 20 % of V_0, which is almost comparable to the maximum velocity in the x-direction of the vortex motion. Therefore, if we assume $(\Delta v_y)_{max} \sim v_{x\ max}$ in the saturation

stage, the condition for the fast shock formation can be simply written as

$$\frac{1}{2} V_O + (\Delta v_y)_{max} \sim \frac{1}{2} V_O + v_{x\,max} > (c_s^2 + v_a^2)^{1/2} \qquad (17)$$

If we use the fact that $v_{x\,max} \lesssim 0.25\ V_O$, we obtain from the above equation

$$M_f > 1.3 \qquad (18)$$

as a rough condition for the fast shock formation. Therefore, for a fast magnetosonic Mach number less than some critical value, say 1.3, the acceleration of the initial flow is not expected to be strong enough to form the fast shock discontinuity.

4.3 Anomalous transport

Let us now investigate anomalous momentum and energy transport by the instabilities. If we take a spatial average of the y-component of (2) in the y-direction, we obtain for the two-dimensional case ($\partial/\partial z=0$) using the periodicity of perturbations in the y-direction

$$\frac{\partial}{\partial t} \langle \rho v_y \rangle = - \frac{\partial}{\partial x} \langle \rho v_x v_y - \frac{B_x B_y}{\mu_0} \rangle \qquad (19)$$

where the brackets denote the spatial average over the wave period. From (19) we find that the instability can exert an anomalous tangential stress $\langle \rho v_x v_y - B_x B_y / \mu_0 \rangle$ on plasma, where the first term is the hydrodynamic Reynolds stress and the second term is the hydromagnetic Maxwell (magnetic) stress. In order to calculate the change of momentum flux in a rectangular volume extending from x=0 to x=∞ and surrounded by a unit surface at x=0, we integrate equation (19) from x=∞ to x=0 to obtain

$$\frac{\partial}{\partial t} \int_{\infty}^{0} \langle \rho v_y \rangle\ dx = - \langle \rho v_x v_y - B_x B_y / \mu_0 \rangle_{x=0} \qquad (20)$$

This indicates that across the surface at x=0 (magnetospheric boundary) there is a net transfer of momentum in the y-direction by the instability, which is equal to the anomalous tangential stress at x=0. In the magnetospheric inertial frame, where the velocity changes from zero to V_O, the net energy flux across velocity shear layer is given by the tangential stress multiplied by V_O.

We show in Figure 11 anomalous stresses (upper panel) normalized by $\rho_O V_O^2$ and velocity shear profiles (lower panel) for the two basic configurations ; the time evolutions for these cases are shown in Figure 3 and the velocity shear profiles are those at their saturation stages. For the transverse configuration ($\underset{\sim}{B_O} \perp \underset{\sim}{v_O}$) assuming two-dimensionality where $\partial/\partial z=0$, i.e., the field line is not allowed to bend, the Maxwell stress vanishes and only the Reynolds stress at $t/\tau=30$ is plotted (dot-dash curve). The anomalous Reynolds stress peaks at x=0, and the peak stress becomes 0.006 $\rho_O V_O^2$, which is 0.6 %

of the flow momentum flux far from the shear layer. This anomalous
momentum transport by the Reynolds stress leads to a finite diffusion
of momentum shown as a relaxation of the velocity profile from dashed
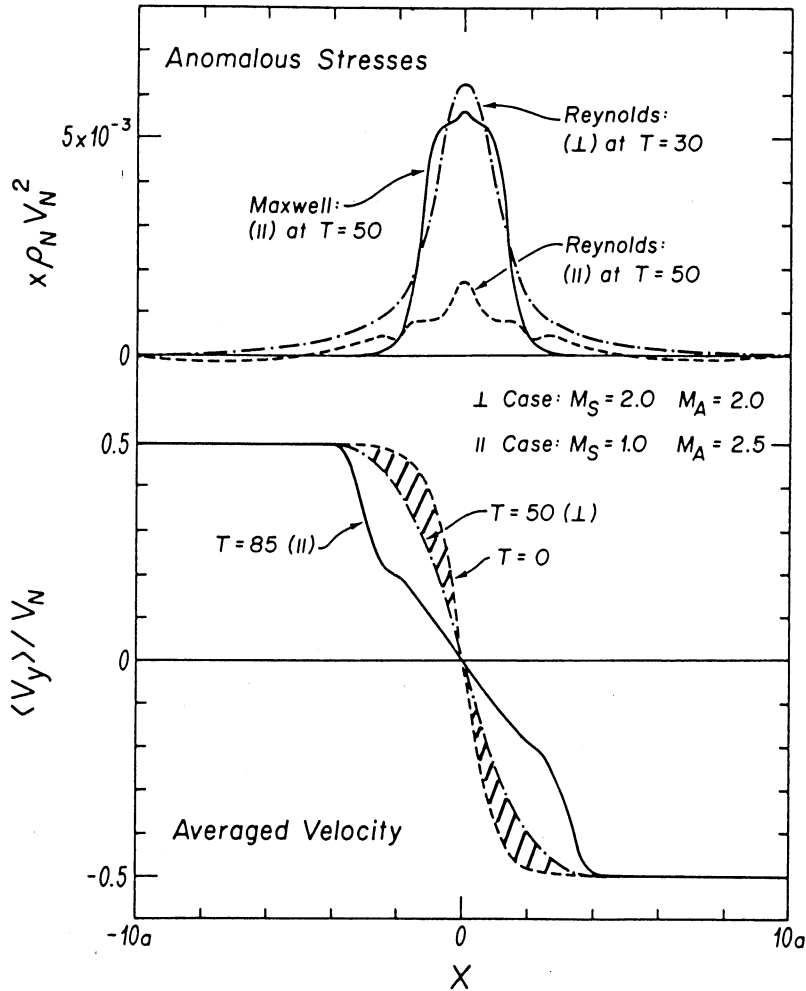curve to dot-dash curve in the lower panel. In the parallel

Figure 11. Spatial averages of v_y at t=0 and in the growing phases
(lower panel) for the parallel (M_S=1.0, M_A=2.5) and
transverse (M_S=M_A=2.0) configurations. Spatial averages of
anomalous stresses for the two configurations (upper
panel). The hatched area corresponds to the momentum
transport for the transverse case.

configuration, the Maxwell stress (solid curve) at t/τ=50 is much
larger than the Reynolds stress (dashed curve), and the Maxwell stress
reaches ~0.5 % of the flow momentum flux at this time far from the
velocity shear layer. Note that the anomalous Maxwell stress is
strongly confined within the region of the velocity shear where the
magnetic field line is bent most strongly; this causes a very strong

relaxation and widening of the initial velocity shear (solid curve in the lower panel), which in turn leads to dynamo amplification of magnetic field. Since the net transfered momentum is proportional to the area between the initial velocity shear profile and the velocity shear profile at the saturation stage (shown by the hatched area for the transverse case), it is seen from the lower panel that the parallel configuration has a larger (about 3 times) momentum transport than the transverse configuration. This means that the hydromagnetic Maxwell stress is more efficient than the hydrodynamic Reynolds stress in the momentum transport. If we define the anomalous viscosity by

$$\nu_{ano} = \rho_N^{-1} \langle B_x B_y / \mu_0 - \rho v_x v_y \rangle \, (d\langle v_y \rangle / dx)^{-1} \tag{21}$$

we obtain for the parallel case ($M_S = 1.0$, $M_A = 2.5$) at $t/\tau = 50$, $\nu_{ano} = 2.6 \times 10^{-2} a V_0$ at $x = 0$, which is mainly due to magnetic stress (magnetic viscosity; Eardley and Lightman, 1978). For the transverse case ($M_S = M_A = 2.0$) we obtain $\nu_{ano} = 1.2 \times 10^{-2} a V_0$ at $x = 0$, $t/\tau = 80$.

These results suggest that the momentum diffusion process is an intrinsic feature of the Kelvin-Helmholtz instabilities which in turn leads to the saturation of the instability. It is interesting to note that the importance of the MHD wave, the Alfvén wave or slow magnetosonic wave in the compressible case, in increasing the diffusion rate of the magnetic field has been recognized by Petchek (1964) and Levy et al., (1964). In the present case, the slow rarefaction wave contributes to the strong diffusion of momentum or dissipation of vorticity as was seen in Figure 11.

5. SUMMARY AND DISCUSSION

We have demonstrated by a MHD simulation that the MHD Kelvin-Helmholtz instabilities leads to finite transport of momentum and energy across the magnetospheric boundary. For both parallel and transverse configurations, important results revealed by the present simulation may be summarized as follows:

Parallel configuration
(1) For super-Alfvénic and transonic shear flow ($M_S = 1, 2.5 < M_A < 4$), the instability leads to the oscillation of the velocity shear layer, which bends the initially uniform magnetic field.
(2) For hyper-Alfvénic shear flow ($M_A > 4$, $M_S = 1$), the instability leads to formation of eddies trapped in a large vortex, and the initially uniform magnetic field is strongly compressed, twisted, and hence amplified with the amplification factor $\sim M_A / 2$ by flow vortices and the total magnetic energy in the whole calculation domain increases by the dynamo action $\underset{\sim}{E} \cdot \underset{\sim}{J} = \underset{\sim}{v} \cdot (\underset{\sim}{J} \times \underset{\sim}{B}) < 0$.
(3) The anomalous momentum and energy fluxes across the velocity shear layer reach to 2% and 4% of those of the background flow far from the shear layer and the initial velocity shear is strongly relaxed by those finite transport.

Transverse configuration
(1) For a magnetosonic mach number larger than a critical value, the instability leads to the formation of the fast shock discontinuity from an initially subfast shear flow due to the acceleration of the flow velocity by a vortex.
(2) The anomalous momentum and energy fluxes across the velocity shear layer reach to 1% and 2% of those of the background flow far from the shear layer.

With regard to the transport of solar wind momentum and energy into the magnetosphere, it has been said that in order to satisfy the energy consumption in the magnetosphere, the necessary momentum flux is 1-2% of the solar wind momentum flux. Therefore, the anomalous momentum flux by the Kelvin-Helmholtz instabilities seems to well satisfy the requirement of the viscous-like interaction hypothesis (Axford and Hines, 1961). For a typical condition at the magnetospheric boundary, $a > \rho_{Li}$ and $V_o \sim v_{ti}$, where ρ_{Li} and v_{ti} are Larmor radius and thermal speed of typical ions at the boundary, the observed anomalous viscosities $\nu_{ano} \simeq 0.02a\ V_o$ for the parallel configuration and $\nu_{ano} \simeq 0.01a\ V_o$ for the transverse configuration become comparable to the Bohm diffusion, which is usually regarded as the upper bound for the anomalous particle transport in the low-β plasma. For typical parameters at the magnetospheric boundary $a = 250$ km, $V_o = 400$ km/sec, these anomalous viscosities also become equal to or larger than the viscosity calculated by Axford and Hines (1961) $\nu_{ano} \simeq 10^{13}$ cm^2/sec to account for the magnetospheric convection with a reasonable intensity. These results based on a MHD simulation of the Kelivn-Helmholtz instabilities strongly suggest that the Kelvin-Helmholtz instabilities play an important role in the transfer of momentum and energy across the magnetospheric boundary, particularly when the magnetic stress (viscosity) by the tangled magnetic field lines is involved in the interaction.

References

Axford, W.I., and C.O. Hines, A unifying theory of high-latitude geophysical phenomena and geomagnetic storms, Can. J. Physics., 39, 1433, 1961.

Eardley, D.M., and A.P. Lightman, Magnetic viscosity in relativistic acceretion disks, Ap.J., 200, 187, 1975.

Landau, L.D., and E.M. Lifshitz, Fluid Mechanics, Pergamon Press, Oxford, p310, 1959.

Lapidus, A., A detached shock calculation by second-order finite differences J. Comput. Phys., 2, 154, 1967.

Levy, R.H., H.E. Petschek, and G.L. Siscoe, Aerodynamic aspects of the magnetospheric flow, AIAAJ., 2, 2065, 1964.

Miura, A., and P.L. Pritchett, Nonlocal stability analysis of the MHD Kelvin-Helmholtz instability in a compressible plasma, J. Geophys. Res., 87, 7431, 1982.

Miura, A., Nonlinear evolution of the magnetohydrodynamic Kelvin-Helmholtz instability, Phys. Rev. Lett., 49, 779, 1982.

Petcheck, H.E., Magnetic field annihilation, NASA Spec. Publ., SP-50, 425, 1964.

Richtmyer, R.D., and K.W. Morton, Difference methods for initial-value problems,2nd ed., Interscience Publishers, New York, 360, 1967.

Table 1. The plasma β at the initial stage, the plasma β at the saturation
         stage of the instability, and the amplification of the magnetic
         field for three different Alfvén mach numbers.

Table 1

M_A	Initial β	β at the saturation stage	B_f/B_i	$\dfrac{W_B - W_B(t=0)}{W_B(t=0)}$
2.5	7.5	1.6	1.9	8.7 %
5.0	30.0	1.7	3.6	26 %
10.0	120.0	2.3	6.0	140 %